Nanocrystals of Platinum-Group Metals as Peroxidase Mimics for *in Vitro* Diagnostics

Zhiyuan Wei, a Zheng Xi, a Sergey Vlasov, a Jasmin Ayala, a and Xiaohu Xia a, b

^aDepartment of Chemistry, University of Central Florida, Orlando, Florida 32816, United States ^bNanoScience Technology Center, University of Central Florida, Orlando, Florida 32816, United States

^{*}Corresponding author. E-mail: Xiaohu.Xia@ucf.edu

Abstract

Peroxidase mimics of nanoscale materials as alternatives to natural peroxidases have found widespread uses in biomedicine. Among various types of peroxidase mimics, platinum-group metal (PGM) nanocrystals have drawn considerable attention in recent years due to their superior properties. Particularly, PGM nanocrystals display high catalytic efficiencies, allow for facile surface modifications, and possess excellent stabilities. This feature article summarizes our recent work on development of PGM nanocrystals as peroxidase mimics and exploration of their applications in *in vitro* diagnostics. We begin with a brief introduction to controlled synthesis of PGM nanocrystals in solution phase. We then elaborate on a variety of physicochemical parameters that can be carefully tuned to optimize the peroxidase-like properties of PGM nanocrystals. Then, we highlight the applications of PGM nanocrystals in different *in vitro* diagnostic platforms. We conclude this article with personal perspectives on future research directions in this emerging field, where challenges and opportunities are remarked.

Table of Contents

The use of carefully engineered platinum-group metal nanocrystals as peroxidase mimics opens a new avenue to development of sensitive *in vitro* diagnostic technologies.

Keywords: platinum group metal · nanocrystal · peroxidase mimic · physicochemical property · catalysis

1. Introduction

Peroxidases (particularly horseradish peroxidase, HRP¹⁻³) have been widely used as a critical component in in vitro diagnostics for decades. 4-8 Notable examples of peroxidases-based immunosorbent assay (ELISA), 9,10 enzyme-linked kits include diagnostic immunohistochemistry, 11-13 and western blot. 14,15 In a typical kit, peroxidases are conjugated to bioreceptors (e.g., antibodies and nucleic acids) and specifically generate detection signal by catalyzing peroxidase substrates. 16,17 Since peroxidases are responsible for signal generation, they largely determine the performance of a diagnostic kit, including detection sensitivity, reproducibility, and stability. The inherit drawbacks of peroxidases greatly limit the upgrade and advancement of *in vitro* diagnostics. For instance, like many other natural enzymes, peroxidases are unstable under harsh conditions (e.g., acidic pH and high temperatures) because they are essentially proteins and, thus, subject to denature and unfolding.¹⁸ The catalytic efficiencies of peroxidases are relatively low as confined by the inherent molecular structures of peroxidases. In addition, isolation and purification of peroxidases from organisms is time and material consuming path.

To overcome the drawbacks of natural peroxidases, nanomaterials with peroxidase-like activities (*i.e.*, peroxidase mimics) were developed and used as alternatives in *in vitro* diagnostics. 19,20 Over the past decade or so, a vast variety of peroxidase mimics that are made of inorganic nanomaterials ranging from carbon $^{21-24}$ to metals, $^{25-27}$ metal oxides, $^{28-31}$ and ceria $^{32-34}$ have been reported. Most peroxidase mimics are much more stable than natural peroxidases. As such, in this field, great effort has been made to improve the catalytic efficiency of peroxidase mimics, which is vital to ensure high detection sensitivity for diagnostics and thus their capabilities of detecting serious diseases at early stages. 19 It should be noted that it is challenging to achieve a substantially improved catalytic efficiency relative to natural peroxidase. The catalytic constant (K_{cat}) measures the catalytic efficiency and is defined as the maximum number of products generated per catalyst per second. 35 The K_{cat} of HRP is at the level of 10^3 s⁻¹. 35 In contrast, K_{cat} values of most peroxidase mimics with sizes of 1-100 nm are only a few orders of magnitude greater than that of HRP.

During the past five years, our research group has been working on the design, development, and synthesis of platinum-group metal (PGM) nanocrystals as peroxidase mimics and exploration of their applications in *in vitro* diagnostics. It was determined to focus on PGM based peroxidase

mimics because of their unique features. First of all, PGM nanocrystals possess higher peroxidase-like catalytic efficiency than most other types of peroxidase mimics. In particular, their catalytic efficiencies can be optimized and enhanced by carefully controlling the physicochemical parameters (which will be discussed later). Moreover, they can be conveniently conjugated with bioreceptors through simple physical adsorption or metal-thiolate bonding. ³⁶⁻⁴⁰ Furthermore, they are ultra-stable owing to the inertness of noble metals. ^{41,42} Lastly, they can be easily synthesized in a common wet chemistry laboratory. With well-documented procedures and knowledge we learn from previous studies, it is now feasible to precisely control their shape, size and composition at the atomic levels during a synthesis. ⁴³⁻⁴⁵ All these features of PGM nanocrystals make them promising candidates of peroxidase mimics with great potential for biomedical applications.

This feature article highlights our recent studies on the development of PGM nanocrystals as peroxidase mimics. We start with a brief introduction of solution-phase synthesis of PGM nanocrystals. We then elaborate how to rationally design PGM based peroxidase mimics of interest by detailing the effects of nanocrystal size, shape, elemental composition, strain, and surface ligands one by one. Afterwards, applications of those PGM based peroxidase mimics in *in vitro* diagnostics are highlighted. In the end, we provide outlook for future research, where challenges and opportunities of PGM based peroxidase mimics are discussed.

2. Solution-phase synthesis of PGM nanocrystals

Solution-phase synthesis, among many synthetic methods, is a powerful means to produce quality colloidal PGM nanocrystals. 46-48 Significantly, the structures of PGM nanocrystals can be finely controlled in the solution-phase synthesis by carefully manipulating the thermodynamic and kinetic parameters. In the most basic solution-phase synthesis system, metal precursor is reduced by a reductant in a solvent in the presence of a colloidal stabilizer. The synthesis can be more complicated when extra components, such as facet-specific capping agents, 49,50 oxidative etchants 11 and other additives, 52-54 are involved. Since comprehensive reviews of solution-phase synthesis can be found in the literature, 55,56 we limit our discussion to key points for design and synthesis of PGM nanocrystals that are suitable to be used as peroxidase mimics for biomedicine.

In most biomedical applications of peroxidase mimics, the mimics are desired to be water soluble.⁵⁷⁻⁵⁹ For this purpose, polar solvents are typically used in the synthesis of PGM nanocrystals as peroxidase mimics. Commonly used polar solvents include water and polyols. Water is the most accessible and economical solvent. In contrast, polyols are relatively expensive,

but more versatile. 60-62 Polyol is a type of a dual-function reagent. It not only acts as a solvent but also serves as a reductant upon heating. 63,64 Remarkably, the reducing power of a polyol can be controlled by reaction temperature, which provides an effective approach to manipulate the reaction kinetics of a synthesis. Taking ethylene glycol (EG) as an example, heating it in air results in its oxidation to glycolaldehyde, a reductant capable of reducing PGM ions. 63 Such oxidation is temperature-dependent, which is the main reason why reducing power of EG is dependent on temperature. Notably, the reducing power of polyol also has a strong dependence on the length of hydrocarbon chain.⁶⁵ In general, a polyol with a longer hydrocarbon chain has weaker reducing power. For instance, under the same temperature, the reducing power of EG, diethylene glycol (DEG) and triethylene glycol (TEG) decreases in the order of EG > DEG > TEG. 66,67 These features ensure polyol an effective and versatile reagent in solution-phase synthesis of PGM nanocrystals. To prepare water-soluble PGM nanocrystals, in addition to polar solvents, hydrophilic colloidal stabilizers are typically used in a synthesis. In general, the stabilizers will bind strongly to the surfaces of PGM nanocrystals through chemisorption after synthesis.⁶⁸⁻⁷¹ Examples of hydrophilic stabilizers include polyvinylpyrrolidone (PVP), 72-74 citrate, 75-77 cetyltrimethylammonium bromide (CTAB), 78-80 and cetyltrimethylammonium chloride (CTAC). 81-83 The stabilizers bound to the surface of PGM nanocrystals (also known as "surface ligands") have significant impact on their peroxidase-like efficiencies, which will be discussed later. Moreover, the type of surface ligands also plays a key role in functionalization of PGM nanocrystals with bioreceptors. 40,84,85

In solution-phase synthesis of PGM nanocrystals, there are two complementary strategies: one-pot synthesis (Figure 1a) and seeded growth (Figure 1b). The production of a nanocrystal from one-pot synthesis experiences several key stages, including generation of atoms, nucleation, transformation from nuclei to seeds, and growth from seeds to nanocrystals.⁵⁵ The stages of nucleation and seed formation play important roles in determining the structure of final nanocrystal. Nucleation represents the very first stage of crystallization process, where clusters of very few metal atoms and/or ions are formed. When a cluster has pasted a critical size at which structural fluctuations become thermodynamically less favorable, it evolves to a seed. Seeds that may take a single crystal, singly twinned, multiply twinned, or a stacking-fault structure hold a decisive role in guiding the growth of nanocrystals.⁸⁶⁻⁸⁹ Nevertheless, it is challenging to understand and control the formation of nuclei and seeds.^{55,90,91} The challenge is imposed by the fact that the processes at

early stages are determined by various thermodynamic (*e.g.*, surface capping) and kinetic (*e.g.*, concentration and temperature) parameters that are intricately entangled to each other. Moreover, current analytical tools are not capable of directly capturing and monitoring clusters of limited atoms and/or ions in real space. Despite of the lack of clear mechanistic understanding, thanks to the experiences and procedures reported by many research groups, it is practically feasible to obtain a variety of PGM nanocrystals with good uniformities and large quantities. ⁹²⁻⁹⁶

In seeded growth (Figure 1b), preformed seeds are added to the synthetic solution. During the synthesis, newly formed atoms resulting from the reduction of metal precursors are deposited on the surface of growing seeds. 43,97-99 The seeds are sizable and can be observed and analyzed by electron microscopes, making it convenient to track and monitor the growth process. Compared to one-pot synthesis, the growth pathway and thus the structure of final nanocrystals in seeded growth are more controllable. In addition, seeded growth is more convenient for synthesis of multimetallic nanocrystals, especially core-shell nanostructures, 100-103 by introducing precursors of different metals. By carefully monitoring the growth process, different roles of thermodynamic and kinetic factors can be understood. As a result, the structure of PGM nanocrystals in seeded growth can be achieved by thermodynamic or kinetic control.

In a thermodynamic control, a powerful and effective approach is to use facet-specific capping agent. Binding of capping agents to a specific facet will lower the surface free energy of that facet. 44,68,104,105 As such, the growth towards the facet is slowed down. Taking the growth of Pd cuboctahedral seed that are encased by both {100} and {111} facets as an example, the presence of Br⁻ ion as a Pd{100}-specific capping agent will force the growth of a seed toward the <111> directions since {100} facets are passivated by Br⁻ ions. Eventually, Pd nanocube with six {100} side facets is obtained as the final product. 106 A similar strategy has been applied to shape-controlled synthesis of many other PGM nanocrystals. 107-109 In recent years, with continuous mechanistic understanding, kinetic control has become a versatile and convenient method for controlled synthesis of PGM nanocrystals. In kinetic control, the key is to manipulate the rates of atom deposition and surface diffusion. Upon the deposition of atoms on specific sites of a growing seed, the adatoms will have chance to migrate to a different site through surface diffusion. 44,104,110 The growth pathway of seed and, thus, the structure taken by final products are primarily determined by the relative rates of atom deposition and surface diffusion. 111 Figure 1c shows two typical growth modes. Specifically, if the rate of surface diffusion is greater than that of atom

deposition, adatoms will spread across the entire surface through surface diffusion. As a result, the growth will proceed by the layer-by-layer mode that features conformal coating of newly added atoms. ^{112,113} On the contrary, if the rate of atom deposition dominates, the growth will follow the island mode, which gives rise to small particles on seed surfaces. Importantly, both atom deposition and surface diffusion are kinetic parameters that can be manipulated by altering the experimental conditions. Practically, to control the growth pathway of a seed, one needs to first identify the sites of atom deposition. In general, such sites are thermodynamically less stable surfaces that have higher surface free energy. Afterwards, the growth can be straightforwardly controlled by manipulating the rates of atom deposition and surface diffusion. ⁴⁴ Over the past several years, we have applied kinetic control to the synthesis of a variety of PGM nanocrystals. Detailed mechanistic understanding and synthetic protocols can be found in our previous publications. ^{111,114-117}

3. Rational design of PGM based peroxidase mimics

The peroxidase-like activities of PGM nanocrystals have strong dependence on their physicochemical parameters, including shape, size, elemental composition, strain, and surface ligand. To design and synthesize a desired PGM based peroxidase mimic, one needs to carefully optimize these parameters. In the following discussion, the roles played by each parameter in determining the peroxidase-like properties of PGM nanocrystals will be specified. Emphasis will be placed on the impact of each parameter on catalytic efficiency in terms of catalytic constant (K_{cat}). All the catalytic efficiencies were determined from apparent steady-state kinetic assays, where the oxidation of 3,3',5,5'-tetramethylbenzidine (TMB, a commonly used peroxidase substrate 118-120) by H₂O₂ that generates blue colored products (*i.e.*, oxidized TMB with λ_{max} at 653 nm³⁵) was used as a model catalytic reaction.

Effect of shape. The shape of PGM nanocrystals plays a significant role in determining their peroxidase-like activities. The shape effect can be understood from two aspects. First, shape correlates to the arrangement of surface atoms that directly influences the interaction of reaction species with metal surface and, thus, the catalytic efficiency. For example, when PGM nanocrystals with a face-centered-cubic (*fcc*) structure take cubic and octahedral shapes, respectively, they expose loosely-packed (100) and closely-packed (111) surfaces. In a previous work by Fang *et al.*, Peroxidase-like catalytic efficiencies of {100}-covered Pd cubes and {111}-covered Pd octahedra were compared under the same conditions. The results indicated Pd cubes

were more catalytically efficient than Pd octahedra, because the homolytic dissociation of H₂O₂ species as the rate-determining step of oxidation of TMB was easier on (100) surface than on (111) surface. In a work by Gao *et al.*, ¹²⁶ Pt concave nanocubes encased by high-index {730} facets were demonstrated to be ~4 times more efficient than Pt nanospheres that were primarily encased by a mixture of {100} and {111} facets.

Second, shape effectively alters the total surface area of a nanocrystal, which has a direct impact on its catalytic efficiency. In general, nanocrystals with open structures (e.g., hollow interiors and branched structures) tend to expose larger surface areas and, thus, possess enhanced catalytic efficiency. In our previous work, 127 we reported Ru nanoframes (Figure 2a,b) that were prepared by selectively depositing Ru atoms on the edges and corners of Pd octahedral seeds, followed by removing Pd through chemical etching. The Ru nanoframes had a small size and ultrathin frames with average edge length and thickness of 6.2 nm and 1.8 nm, respectively. The open structure and fully accessible surfaces ensured a high peroxidase-like efficiency for the nanoframes. The catalytic efficiency in terms of K_{cat} of the nanoframes were determined to be 1.26 \times 10⁴ s⁻¹, which is three times greater than $K_{\rm cat}$ of HRP (4.0 \times 10³ s^{-1 ref}). In a more recent work, ¹²⁸ we demonstrated Pd-Ru core-shell nanostructures with highly porous structure on the surface (Figure 2c,d) that were synthesized by growing Ru on Pd nanocubes as seeds. The key to achieve a porous structure was to ensure that the rate of Ru atom deposition on corner sites of Pd cubic seeds was sufficiently higher than the rate of adatom surface diffusion. The Pd-Ru porous nanocrystals with enlarged surface areas exhibited an outstanding peroxidase-like activity with $K_{\rm cat}$ as high as $4.8 \times 10^5 \, {\rm s}^{-1}$. Similar idea of surface area enlargement through shape control was reported in the cases of Pt nanoparticles with rough surfaces 129 and Pt hollow nanoparticles with both inner and outer surfaces. 130

Effect of size. It is well-documented that particle size plays a critical role in determining the catalytic activities of nanocatalysts in traditional reactions, such as oxygen reduction reaction and hydrogenation reactions. With the change of particle size (especially in the range of 1-10 nm), the ratio of atoms on particle surfaces including faces, edges and corners to interior bulk atoms varies dramatically. Such variations can substantially change the catalytic activities of nanocatalysts. Despite of the demonstrations in traditional catalytic reactions, comprehensive studies on size effect in the niche field of peroxidase mimic research have not been extensively reported. The major difficulty in investigating the size effect might be the challenge to craft

peroxidase mimics having different sizes, but the same morphologies and surface properties.

In the very recent work, 137 we systematically investigated the size effect by using Pd-Ir coreshell nanoparticles (NPs) of different sizes as models. The Pd-Ir NPs were prepared by coating a conformal layer of Ir on the surface of Pd truncated octahedra as seeds, where the thickness of Ir layer was fixed to ~0.55 nm (2-3 atomic layers). The sizes of Pd-Ir NPs were conveniently controlled by using Pd seeds of different sizes. 138 Figure 3a-d shows transmission electron microscopy (TEM) images of Pd-Ir NPs with average sizes of 3.3, 5.9, 9.8 and 13.0 nm. The Pd-Ir NPs of each size had steady uniformities. It should be noted that all the Pd-Ir NPs were primarily covered by Ir{111} facets because Ir was deposited on Pd octahedral seeds following a layer-bylayer mode. Moreover, all the Pd-Ir NPs were covered by the same surface ligand poly(vinylpyrrolidone) (PVP) – on the surface as evidenced by the X-ray photoelectron spectroscopy (XPS) data. Taken together, these Pd-Ir NPs had different sizes, but the same shape, Ir coating and surface properties, could serve as an ideal system to study the size effect in peroxidase mimic mediated catalysis. As summarized by Figure 3e, as the sizes of Pd-Ir NPs increased from 3.3 nm to 13.0 nm, their catalytic efficiencies in K_{cat} continuously increased from 9.4×10^4 to 1.2×10^6 s⁻¹. To better understand the size effect, we compared their area-specific catalytic efficiencies ($K_{\text{cat-specific}}$, which was derived by normalizing the value of K_{cat} against the total surface area of an individual catalyst¹¹⁵). As shown by Figure 3f, K_{cat-specific} values were similar for Pd-Ir NPs with sizes of 3.3-9.8 nm. The K_{cat-specific} value slightly decreased when particle size had increased to 13.0 nm. These results suggested the increased K_{cat} for Pd-Ir NPs of larger sizes (Figure 3e) is primarily because of the enlarged catalytic surface areas that can interact with more substrates during catalysis.

This work represents the first attempt for systematical investigation of size effect in peroxidase mimics. Size effect of other peroxidase mimics deserves thorough exploration in the future, given that the conclusions drawn from Pd-Ir NPs may not be applicable to other types of peroxidsae mimics. Such research is not only fundamentally important, but also practically useful. For example, we have demonstrated that size matters for the application of those 3.3-13.0 nm Pd-Ir NPs (Figure 3a-d) in the enzyme-linked immunosorbent assay (ELISA) platform, where smaller nanoparticles were found to offer higher detection sensitivities. In another example, the performance of Pt nanoparticles as peroxides mimics in lateral flow assay (LFA) platform was demonstrated to have a strong dependence on particle size, where the optimal size was found to be

 $\sim 150 \text{ nm.}^{129}$

Effect of elemental composition. Both experimental data and theoretical simulations have demonstrated that the peroxidase-like activity of PGM nanocrystals has strong dependence on the elemental compositions, especially compositions on the surfaces (1-5 atomic layers).

In our previous study,¹¹⁵ we demonstrated that the catalytic efficiency of Pd nanocube could be dramatically enhanced by coating an ultrathin Ir skin of a few atomic layers on the surface. The resultant Pd-Ir core-shell cubes (Figure 4a,b) display outstanding catalytic efficiency with a K_{cat} value as high as $1.9 \times 10^6 \text{ s}^{-1}$. In contrast, the initial Pd nanocubes only had a K_{cat} in the regime of 10^4 s^{-1} . Significantly, we found Ir content on Pd surface played a critical role in determining the catalytic efficiency of Pd-Ir cubes. As shown by Figure 4c, a volcano-shaped relationship was observed between K_{cat} values and Ir contents. The maximum point was found at the Ir/Pd ratio of 0.062, which corresponds to roughly a single atomic layer of Ir on Pd cube surface. We also performed density functional theory (DFT) simulations to understand the observed composition-dependent catalytic efficiency. Four model surfaces – pure Pd(100), single Ir overlayer on Pd(100), three Ir overlayers on Pd(100), and pure Ir(100) surfaces – were constructed. Adsorption energies of key species in the catalytic reaction on these four type of surfaces were calculated. The calculation results suggested that adsorption energies were most exothermic on the single Ir overlayer on Pd(100) surface, indicating that it was the most reactive surface among the four. This result was consistent with the experimental observation shown in Figure 4c.

In another study, ¹¹⁷ we demonstrated that Au nanoparticles (AuNPs) could be endowed with strong peroxidase-like activity by coating thin layers of Pt (1-10 atomic layers) on their surfaces. Note that pristine AuNPs possess outstanding plasmonic activities but weak peroxidase-like activities. By forcing the growth of Pt on AuNPs to follow a layer-by-layer mode, Au-Pt_{nL} coreshell NPs (nL: n atomic layers of Pt) as products were synthesized. The thickness of Pt shell could be conveniently and precisely controlled at 1-10 atomic layers (n = 1-10) by adjusting the amount of Pt precursor. As an example, Figure 4d,e show the morphology and compositions of Au-Pt₄L NPs. As summarized in Figure 4f, the catalytic efficiency of Au-Pt_{nL} NPs has a strong dependence on the number of Pt atomic layers (n). The initial AuNPs (n = 0) had a very low K_{cat} at the level of 10^3 s⁻¹. K_{cat} values of Au-Pt_{nL} NPs increased dramatically as n increased from 1-3, reaching the regime of 10^6 s⁻¹. Thereafter ($n \ge 4$), the K_{cat} value become saturated. To understand the Pt layer-dependent catalytic efficiency, we derived the d-band center positions of Au-Pt_{nL} surfaces, which

are good measurements for binding affinities toward adsorbates and thus the catalytic efficiencies. The d-band center of Au(111) surface was narrower and had a much lower density near the Fermi level relative to those of Au-Pt_{nL}(111) surfaces, suggesting Au(111) was less catalytically active than Au-Pt_{nL}(111) surfaces. For Au-Pt_{nL}(111) surfaces with n = 1-10, substantial change of d-band center positions was only observed when n increased from 1 to 3. This result suggested that a significant change of catalytic activity of Au-Pt_{nL}(111) should be expected in the range of n = 1-3. These simulation data were consistent with the experimental results shown in Figure 4f.

These examples demonstrate that a subtle alternation in elemental composition on the surface can appreciably change the catalytic efficiency. This observation gives scientists a clue that precisely controlled synthesis of PGM nanocrystals is critical in optimizing their peroxidase-like activities. Fortunately, with increased mechanistic understanding on nanocrystal synthesis and rapid advancement of characterization tools, it is now feasible to design and engineer PGM nanocrystals at the atomic precision.⁴⁴

Effect of strain. Surface strain is oftentimes involved in PGM nanocrystals, which is generally caused by intrinsic twin structures or lattice mismatch between different components of a nanocrystal. Surface strain can modify the surface electronic structure, and thus alter the interaction between catalytic reaction intermediates and surface, which in turn affects the catalytic activity of a catalyst. ^{139,140} In conventional heterogeneous catalysis, engineering surface strain has been proven to be an effective strategy to enhance the activity of a catalyst. Notable examples include CO₂ reduction, ¹⁴¹ oxygen reduction ¹⁴² and formic acid oxidation. ¹⁴³ Nevertheless, in the field of peroxidase mimic research, study of strain effect has not been reported until our recent work.

Specifically, we constructed an ideal system based on Pd octahedra (Figure 5a) and Pd icosahedra (Figure 5b) to investigate the strain effect on the peroxidase-like catalytic efficiency. 144 These two types of Pd nanostructures were designed to have the same Pd{111} facet exposure and capping agent on the surface, similar sizes, surface areas and ligand coverage densities but different surface strains. High-resolution TEM and X-ray diffraction (XRD) analyses indicated the coexistence of apparent tensile and compressive strains on icosahedral facets. In comparison, the strain on octahedral facets is not significant. The strains on both nanostructures were also mapped using geometric phase analysis (GPA 145,146), as shown in Figure 5c,d. Compared to octahedron, icosahedron amplified the surface strain field with half of the surface exhibiting the compressive

strain and the other half exhibiting tensile strain. Representative linear strain scans for the octahedron and icosahedron were shown in Figure 5e and f, respectively. The area-specific catalytic efficiency ($K_{\text{cat-specific}}$) value of Pd icosahedra was determined to be $3.0 \times 10^2 \text{ s}^{-1} \text{ nm}^{-2}$, twice higher than that of Pd octahedra (Figure 5g). Obviously, the enhanced catalytic efficiency of Pd icosahedra can be ascribed to the amplification of surface strain fields. To understand the correlation between the enhanced catalytic efficiency and strained Pd icosahedron surface, we performed DFT simulations to investigate the mechanism of H_2O_2 decomposition and formation of OH radical (a key intermediate for the catalysis). The outcome of our simulation is summarized in Figure 5h, where tensile strain was found to be more beneficial to OH radial generation than compressive strain. Combining the results of GPA analysis (Figure 5c-f) and simulation (Figure 5h), the icosahedron was expected to be 2.5 times more active in generating OH radicals than the octahedron. This calculation agreed well with the experimental measurements (2 times).

In conclusion, we demonstrated that Pd icosahedra are more active than Pd octahedra in catalysing peroxidase substrates and the reason is that icosahedra amplify the surface stain field. To the best of our knowledge, this is the first report of strain effect in nanoscale artificial enzyme development. It is worth investigating strain effect in other enzyme mimic systems. We hope this study can inspire future research directions in this field.

Effect of surface ligand. As discussed in Section 3, PGM nanocrystals obtained from a solution-phase synthesis often have stabilizers or capping agents on the surface (*i.e.*, surface ligands). In general, the ligands bind strongly to nanocrystal surfaces through chemisorption and cannot be easily washed away in solutions. Therefore, it is important to consider the effect of surface ligand on peroxidase-like activities of PGM nanocrystals.

In a recent work, ¹⁵⁰ we investigated the role of surface ligand by focusing on Pt nanocubes that are primarily covered by {100} facets (Figure 6a). We demonstrated that the peroxidase-like activity of Pt nanocubes is influenced by both the type and coverage density of surface ligands. Firstly, we found that CTAB-capped Pt cubes displayed a much lower catalytic efficiency compared to PVP₅₅ (MW $\approx 55,000$)-capped Pt cubes. The $K_{\text{cat-specific}}$ values for the CTAB- and PVP₅₅-capped Pt cubes were determined to be $1.0 \times 10^3 \, \text{s}^{-1} \, \text{nm}^{-2}$ and $2.5 \times 10^3 \, \text{s}^{-1} \, \text{nm}^{-2}$, respectively. The difference in catalytic efficiency can be explained by the molecular conformation of surface ligands. Specifically, CTAB tends to form a compact bilayer on Pt surface. ^{151,152} Therefore, the binding of CTAB somehow blocked Pt surface, making it less accessible to peroxidase substrates.

In comparison, PVP is loosely packed on Pt surface, 39 resulting in the exposure of more active surfaces for the catalysis. Secondly, we found the catalytic efficiency was also influenced by the packing density of surface ligands. Specifically, we compared the catalytic efficiencies of PVP55-, PVP10 (MW $\approx 10,000$)-, and PVP360 (MW $\approx 360,000$)-capped Pt cubes. As summarized in Figure 6b, $K_{\text{cat-specific}}$ values for these three types of cubes increased in the order of: PVP10-capped cubes < PVP55-capped cubes < PVP360-capped cubes. This observed trend can be explained by the packing density of PVP molecules on Pt surface. 153,154 Based on thermal gravimetric analysis, 155 packing densities for PVP10, PVP55, and PVP360 were estimated to be 1.30, 1.19, and 0.87 nm⁻², respectively. As the PVP packing density decreased, the accessibility of substrates to Pt surface was expected to increase, resulting in the increase of catalytic efficiency.

It should be mentioned that surface ligand can also influence the surface functionalization of peroxidase mimics in addition to catalytic efficiency. Particularly, in biomedical applications of peroxidase mimics, one should consider the impact of surface ligand on conjugation of bioreceptors. For instance, citrate-capped PGM nanocrystals can be easily functionalized with antibodies through non-covalent interactions (*e.g.*, ionic and hydrophobic attractions), ^{156,157} while covalent methods are needed for conjugation of PVP-capped nanocrystals with antibodies. ^{85,115,158} In our previous study, we have demonstrated that the type of surface ligand has a significant impact on the efficiency of PEGylation on metal nanoparticles. ⁴⁰

4. Application of PGM based peroxidase mimics in in vitro diagnostics

The outstanding peroxidase-like efficiencies and excellent stabilities of PGM nanocrystals make them suitable as labels for *in vitro* diagnostic applications. In the past five years, we have been actively exploring the application of PGM nanocrystals in various diagnostic platforms. In the following discussion, we will focus on their applications in enzyme-linked immunosorbent assay (ELISA) and lateral flow assay (LFA) as two representative platforms. For consistency, we will highlight those examples with the detection of the same target analyte – human prostate specific antigen (PSA, a prostate cancer biomarker^{159,160}). In the end of this section, we will showcase some signal amplification techniques that can further enhance the detection sensitivity.

Application in ELISA. ELISA has been widely used in research labs and for clinical diagnostics for decades. ¹⁶¹⁻¹⁶³ In a typical ELISA, analyte is quantified through the detectable color signal generated from peroxidase-catalytzed reactions, where enzymes (in most cases, HRP) are conjugated to antibodies specific to the analyte (see Figure 7a). ¹⁶⁴ Despite the broad applications

of ELISA, their limit of detection has not been significantly improved over the years. Since peroxidases are the driving force for detection signal generation, they largely determine the sensitivity of ELISA. An effective approach to enhance the sensitivity of ELISA is to substitute peroxidases with peroxidase mimics.

In our previous work, 115 we have applied Pd-Ir cubes (sample in Figure 4a) to ELISA of PSA. As shown by Figure 7a, the detection principle of the Pd-Ir cubes based ELISA (Pd-Ir ELISA) is essentially the same as conventional HRP ELISA except for the substitution of HRP with Pd-Ir cubes. Herein, goat anti-mouse IgG was conjugated to Pd-Ir cubes using a covalent method, where HS-PEG₃₄₀₀-COOH was used as the linker. By using the same set of antibodies and materials, we compared the performance of Pd-Ir and HRP ELISAs by detecting PSA standards. Figure 7b shows the photograph of the detection results in a 96-well microtiter plate, where the yellow-colored products (i.e., diamine, $\lambda_{\text{max}} \approx 450 \text{ nm}^{118}$) were yielded by quenching the catalytic oxidation of TMB by H₂SO₄. ¹⁶⁵ Clearly, Pd-Ir ELISA provided stronger detection signal. After quantification of the colored solutions using a plate reader, calibration curves were generated for both ELISAs. As shown by Figure 7c, the Pd-Ir ELISA displayed a sigmoid curve regression between the logarithms of PSA concentrations and absorbance, with a broad and quality linear relationship in the range of 2-1,200 pg/mL PSA. A good reproducibility was observed with coefficients of variation (CVs) $\leq 11.8\%$ across the entire concentration range. The limit of detection, as defined by the 3SD method, ¹⁶⁶ was determined to be 0.67 pg/mL. In comparison, the limit of detection of the HRP ELISA was determined to be 75 pg/mL, ~110-fold higher than that of Pd-Ir ELISA. The substantially enhanced detection sensitivity for the Pd-Ir ELISA was due to the significantly higher catalytic efficiency of Pd-Ir cubes relative to HRP since both ELISAs were performed under the same conditions.

This study demonstrated the effectiveness of PGM nanocrystals as peroxidase mimics in ELISA application. The nanocrystals-based ELISA is a promising candidate for ultrasensitive detection of disease biomarkers, of which sensitivity rivals the limits of fluorescent methods. Significantly, it is straightforward to apply the nanocrystals to ELISA, where they are used in a similar way as enzymes. The existing materials, instrument and procedures for conventional ELISA are all adopted in the nanocrystals based ELISAs, making it practically feasible to upgrade the ELISA technology. Using the similar detection principle shown in Figure 7a, we have also demonstrated the application of other PGM nanocrystals in ELISA, including Pd-Ir octahedra and

Pd octahedra and icosahedra. 144

Application in LFA. LFA is one of a handful of diagnostic technologies that can be used outside the laboratory, performed by an untrained person, and determined with the naked eyes without the use of any instrument. 167-169 The most familiar example of LFA might be the home pregnancy test that became available in the market in the 1980s. Most commercial LFAs use Au nanoparticles (AuNPs) of ~40 nm as colorimetric labels because the AuNPs can offer intense red color signal due to a phenomenon known as localized surface plasmon resonance (LSPR). 170-173 As shown by Figure 8a, a typical LFA test strip is assembled by pasting a set of wettable materials on a plastic backing card, where capture antibodies and AuNP-detection antibody conjugates are pre-loaded on the strip. In the presence of analyte, AuNPs will be captured and immobilized on the test line. The accumulation of AuNPs in the test line region will collectively display a red color, of which intensity is correlated to the concentration of analyte in a sample. Note, a control line is designed to indicate if the test is valid.

The bottleneck of LFA technology has been its relatively low sensitivity, which inhibits many critical applications such as early detection of severe infectious diseases. Since the detection signal of AuNPs based LFA (AuNP LFA) originates from the plasmonics of AuNPs, the detection sensitivity is essentially confined by the inherent plasmonic activity of AuNPs. In our recent work, we reported a new approach to circumvent the confinement of AuNP plasmonics and thus substantially enhance the sensitivity of LFA. Specifically, in this approach, we coated conventional AuNPs with a conformal, thin shell of Pt to form Au-Pt core-shell NPs. So long as the Pt shell is ultrathin (<10 atomic layers), the intrinsic plasmonic activity of AuNPs will be retained. On the other hand, Pt shell on the surface will endow the Au-Pt NPs with strong peroxidase-like activity, allowing them to generate secondary (relative to the inherent red color from Au plasmonics) blue color signal by catalyzing the oxidation of TMB by H₂O₂. Significantly, the blue color from catalysis is several orders of magnitude stronger than the red color from plasmonics. The dual functionalities – catalysis and plasmonics – make Au-Pt NPs extremely suitable for LFA. Using Au-Pt_{4L} NPs (4L: 4 atomic layers of Pt; i.e., sample in Figure 4d) as an example, they can offer two different detection alternatives for LFA (see Figure 8a): a low-sensitivity mode with red color produced from AuNP plasmonics and a high-sensitivity mode with blue color generated from Pt shell-mediated catalysis, achieving a "on-demand" tuning of the detection. The low-sensitivity mode is faster and more convenient, while the high-sensitivity mode is more sensitive but involves an additional 5-minute TMB substrate treatment process.

Using PSA as a model disease biomarker, the performance of conventional AuNP LFA and Au-Pt_{4L} NP LFA were compared. As shown by Figure 8b, a similar detection limit by the naked eyes (~2,000 pg/mL) was observed for AuNP LFA and Au-Pt_{4L} NP LFA at low-sensitivity mode. In contrast, under high-sensitivity mode, the naked eye detection limit of Au-Pt_{4L} NP LFA achieved a level as low as 20 pg/mL. Figure 8c compares the calibration curves of the LFAs that were generated by quantifying the color signal intensities. An ultralow limit of detection (3.1 pg/mL) was determined for Au-Pt_{4L} NP LFA at high-sensitive mode, along with a quality linear range at 10-200 pg/mL. In comparison, the limits of detection of AuNP LFA and Au-Pt_{4L} NP LFA at low-sensitive mode were determined to be 272 and 322 pg/mL, respectively.

These results demonstrated that the Au-Pt_{4L} NPs with peroxidase-like activities could enhance the detection sensitivity of conventional LFA by approximately 100 times, enabling it to rival the sensitivities of instrument-based technologies (*e.g.*, ELISA). Such a substantial enhancement is only paid by a simple, 5-minute substrate treatment process at room temperature. A similar idea of using PGM nanocrystals as peroxidase mimics for LFA has been demonstrated by other research groups. ^{129,174}

Signal amplification techniques. To further enhance the detection sensitivity of PGM nanocrystals-based assays, one effective strategy is to amplify the color signal produced from catalytic reactions.

As an example, we have developed an efficient signal amplification system that provided substantial improvement in detection sensitivity for ELISA. 175 As diagramed in Figure 9a, the amplification system is based on the release of a plenty of sub-10 nm Pd-Ir NPs as peroxidase mimics that were pre-loaded in the hollow interiors of gold vesicles (GVs, Figure 9b). Specifically, Pd-Ir NPs encapsulated GVs (referred to as "Pd-Ir NPs@GVs") are used as alternatives to HRP in ELISA. The GVs were prepared by assembling AuNPs with temperature-responsive polymers. Upon heating (> 70 °C), the GVs will be broken up, liberating a large amount of individual Pd-Ir NPs (see Figure 9c) that can generate intense color signal by catalyzing peroxidase substrates. This amplification system is highly efficient due to its unique features: *i*) Pd-Ir NPs as peroxidase mimics are approximately 28-fold more efficient than HRP in generating colored products, providing enhanced color signal; *ii*) the loading capacity of Pd-Ir NPs is maximized by taking the large interior 3D space of the GVs as carriers. In contrast, in most existing amplification systems,

enzymes or mimics are loaded on the 2D surfaces of a carrier; *iii*) the loading of free Pd-Ir NPs in the pocket of GVs avoids the loss of catalytic activity caused by surface modifications/conjugations; *iv*) Pd-Ir NPs are water-soluble and can disperse in catalytic reaction solution upon release, making them much more active than catalysts immobilized on solid surfaces, which is the case for conventional ELISA designs. Taken together, the Pd-Ir NPs@GVs are expected to be able to serve as highly efficient labels for sensitive ELISA. As shown by Figure 9d, using PSA as a model analyte, the Pd-Ir NPs@GVs based ELISA achieved an outstanding performance with an ultralow detection limit. A broad linear range was observed at 0.2-200 pg/mL PSA. Relatively low coefficients of variation across the entire concentration range (≤12.2%) suggested a good reproducibility of the assay. The limit of detection was determined to be 31 fg/mL. For comparison, we also determined the limit of detection for conventional HRP based ELISA that was assembled by using the same set of antibodies and procedures except for the omission of heat treatment process. The limit of detection of HRP ELISA was calculated to be 48 pg/mL, which was ~1,500 times higher than the Pd-Ir NPs@GVs based ELISA. Notably, the Pd-Ir NPs@GVs based ELISA is also much more sensitive than the Pd-Ir cubes based ELISA (Figure 7).

In another example, ¹⁷⁶ we developed a signal amplification technique based on a different mechanism. The amplification technique is called "non-enzyme cascade amplification (NECA)", as shown in Figure 10a. The NECA lies in a cascade amplification system: i) Hundreds of thousands of Ag atoms in a single Ag nanoparticle (~20 nm, in this case) can be converted to Ag+ ions through etching by H₂O₂ and released to aqueous solution; ii) As demonstrated in our previous study, ¹⁷⁷ Ag⁺ ions could efficiently and specifically inhibit the peroxidase-like catalytic activity of Pt nanocubes. A single Ag^+ ion could inhibit the generation of $\sim 10^4$ colored molecule (i.e., oxidized TMB) within several minutes. Combined, the detection signal, which refers to the diminished color signal relative to a control, could be amplified by orders of magnitude in the NECA system. By functionalizing Ag nanoparticles with antibodies, the NECA can be conveniently used for detection of disease biomarkers in a similar fashion as conventional ELISA (see Figure 10a). As shown by Figure 10b, the NECA assay achieved a low limit of detection of 0.165 pg/mL of PSA, along with a quality linear range at 2-64 pg/mL of PSA and coefficients of variation <10%. In comparison, the limit of detection for HRP ELISA that used the same set of antibodies was determined to be 16 pg/mL. These results suggested that the NECA system could enhance the detection sensitivity by two orders of magnitude as compared to conventional HRP ELISA. It is

worth noting that the sensitivity of NECA assay could be further enhanced by coupling with silver enhancement technique that was able to amplify the size of Ag nanoparticles attached to antibodies. The limit of detection for the silver enhancement coupled NECA assay was as low as 0.031 pg/mL of PSA.

These examples demonstrated that the detection sensitivity of peroxidase mimics-based assays could be enhanced by integrating signal amplification techniques. More effective and robust ways to amplify the signal deserve further exploration in the future. An ideal signal amplification technique is expected to enable ultrasensitive detection without involving additional instrument and complicated assay procedures.

5. Conclusions and Outlook

In this feature article, PGM nanocrystals as a type of highly efficient and versatile peroxidase mimics and their applications in *in vitro* diagnostics were discussed. Their peroxidase-like activities can be tuned and optimized by carefully controlling the physiochemical parameters, including particle shape, size, elemental composition, strain and chemical ligands on the surface. The outstanding catalytic activities, along with excellent stabilities and facile surface modification, make PGM nanocrystals particularly suitable as colorimetric labels for applications in *in vitro* diagnostics. Compared to natural peroxidases-based assays, PGM nanocrystals-based assays offer substantially improved detection sensitivities. Their sensitivity could be further enhanced by integrating signal amplification techniques. Importantly, the PGM nanocrystals based diagnostic platforms are compatible with the instrument and procedures of existing natural enzymes-based technologies, making it straightforward to apply them to practical uses.

Despite great progresses on the development of PGM based peroxidase mimics have been made in recent years, there are quite a few challenges and opportunities in this emerging field: *i*) Mechanistic understanding. Although the catalytic activities of PGM nanocrystals were found to have strong dependence on the physicochemical parameters, the explicit catalytic mechanisms on nanocrystal surfaces are not clearly understood. Future theoretical simulations along with advanced analytical tools that are capable of monitoring and analyzing the catalytic reaction *in situ* may offer more insights into the structure-property relationships; *ii*) Catalytic activity *versus* stability. While the catalytic activity of PGM nanocrystals is enhanced, the stability of active sites need to be considered. For instance, sharp corners, ¹⁷⁸ twin boundaries, ¹⁷⁹ and thin shells ¹⁸⁰ of a nanocrystal are beneficial to their catalytic activity. The stability of these elegant sites deserves

careful investigation; ¹⁸¹ *iii*) Specificity. Compared to natural peroxidases, PGM nanocrystals as peroxidase mimics have relatively poor specificities. For example, most PGM nanocrystals possess both peroxidase- and oxidase-like properties, and many other catalytic activities. ^{125,182,183} One needs to consider and avoid non-specific signal in certain applications; *iv*) Nanocrystal uniformity. Good uniformity, in terms of all types of physicochemical parameters, is the basis of the reproducibility and reliability of PGM nanocrystals-based applications. It is challenging and important to produce PGM nanocrystals with excellent uniformities, especially for nanocrystals obtained from different batches of synthesis; *v*) Scale-up synthesis. Synthesis of PGM nanocrystals with large scales and high qualities has been a challenge. Recent work on droplet reactors may open an avenue to scale-up synthesis of PGM nanocrystals, enabling extensive use of them in various applications; ^{184,185} *vi*) Potential toxicity. Comprehensive studies on potential toxicities of PGM nanocrystals as peroxides mimics have been rarely reported. This research subject is significant to ensure safe and sustainable use of PGM nanocrystals in certain applications. We hope this article can serve as a useful resource to inspire valuable basic and applied research in this field.

Conflict of Interest

There are no conflicts to declare.

Acknowledgments

This work was supported in part by the grants from the National Science Foundation (CHE-1834874, CEBT-1804525, and DMR-2004546), the National Institute of Food and Agriculture, U.S. Department of Agriculture (2020-67021-31257), and the startup funds from University of Central Florida (UCF).

Notes and references

- 1 R. Huang, N. Hu, *Bioelectrochemistry*, 2001, **54**, 75-81.
- 2 D. Ribatti, *Milestones in Immunology*, Academic Press, Cambridge, 2017.
- 3 T. L. Lewis, K. A. Roth, *Pathobiology of Human Disease*, Academic Press, Cambridge, 2014.

- 4 A. M. Azevedo, V. C. Martins, Duarte M.F. Prazeres, V. Vojinović, J. M.S. Cabral, L. P. Fonseca, *Biotechnol. Annu. Rev.*, 2003, **9**, 199-247.
- 5 N. C. Veitch, *Phytochemistry*, 2004, **65**, 249-259.
- 6 F. W. Krainer, A. Glieder, Appl. Microbiol. Biotechnol., 2015, 99, 1611-1625.
- 7 A. K. M. Kafi, G. Wu, A. Chen, *Biosens. Bioelectron.*, 2008, **24**, 566-571.
- 8 M. A. A. Lomillo, J. G. Ruiz, F. J. M. Pascual, Anal. Chim. Acta., 2005, 547, 209-214.
- 9 A. V. Vlassov, S. Magdaleno, R. Setterquist, R. Conrad, *Biochim. Biophys. Acta.*, 2012, 7, 940-948.
- 10 J. R. Crowther. The ELISA guidebook, 2nd ed, Humana Press, Totowa, 2008.
- 11 J. A. Ramos-Vara, Vet. Pathol., 2005, 42, 405-426.
- 12 S. K. Ludwin, J. C. Kosek, L. F. Eng, J. Comp. Neurol., 1976, 165, 197-207.
- L. A. Sternberger, P. H. Hardy JR, J. J. Cuculis, H. G. Meyer, *J. Histochem. Cytochem.*, 1970,
 18, 315-333.
- 14 T. Mahmood, P. Yang, N. Am. J. Med. Sci., 2012, 4, 429-434.
- 15 B. T. Kurien, R. H. Scofield, *Methods*, 2006, **38**, 283-293.
- 16 R.M. Lequin, Clin. Chem., 2005, **51**, 2415-2418.
- 17 C. P. Price, D. J. Newman (Eds.), *Principles and Practice of Immunoassay, 2nd ed.*, Stockton, New York, 1997.
- 18 K. Chattopadhyay, S. Mazumdar, *Biochemistry*, 2000, **39**, 263-270.
- 19 H. Wei, E. Wang, Chem. Soc. Rev., 2013, 42, 6060-6093.
- 20 J. Wu, X. Wang, Q. Wang, Z. Lou, S. Li, Y. Zhu, L. Qin, H. Wei, Chem. Soc. Rev., 2019, 48, 1004-1076.
- 21 M. Liu, H. Zhao, S. Chen, H. Yu, X. Quan, ACS Nano, 2012, 6, 3142-3151.
- 22 Y. Song, K. Qu, C. Zhao, J. Ren, X. Qu, Adv. Mater., 2010, 22, 2206-2210.
- 23 W. Shi, Q. Wang, Y. Long, Z. Cheng, S. Chen, H. Zheng, Y. Huang, *Chem. Commun.*, 2011, 47, 6695-6697.
- 24 H. Sun, Y. Zhou, J. Ren, X. Qu, Angew. Chem. Int. Ed., 2018, 57, 9224-9237.
- 25 M. Ma, Y. Zhang, N. Gu, Colloids. Surf. A Physicochem. Eng. Asp., 2011, 373, 6-10.
- 26 J. Fan, J. Yin, B. Ning, X. Wu, Y. Hu, M. Ferrari, G. J. Anderson, J. Wei, Y. Zhao, G. Nie, *Biomaterials*, 2011, 32, 1611-1618.
- 27 W. He, X. Wu, J. Liu, X. Hu, K. Zhang, S. Hou, W. Zhou, S. Xie, *Chem. Mater.*, 2010, 22,

- 2988-2994.
- 28 C. Ray, S. Dutta, S. Sarkar, R. Sahoo, A. Roy, T. Pal, J. Mater. Chem. B, 2014, 2, 6097-6105.
- 29 R. André, F. Natálio, M. Humanes, J. Leppin, K. Heinze, R. Wever, H-C Schröder, W. EG Müller, W. Tremel, *Adv. Funct. Mater.* 2011, **21**, 501-509.
- 30 H. Zhao, Y. Dong, P. Jiang, G. Wang, J. Zhang, ACS Appl. Mater. Inter., 2015, 7, 6451-6461.
- 31 H. Wei, E. Wang, Anal. Chem., 2008, 80, 2250-2254.
- 32 Z. Tian, J. Li, Z. Zhang, W. Gao, X. Zhou, Y. Qu, Biomaterials, 2015, 59, 116-124.
- 33 W. Guo, M. Zhang, Z. Lou, M. Zhou, P. Wang, H. Wei, *ChemCatChem*, 2019, 11, 737-743.
- 34 Q. Liu, Y. Yang, X. Lv, Y. Ding, Y. Zhang, J. Jing, C. Xu, Sens. Actuators B Chem., 2017, **240**, 726-734.
- 35 L. Gao, J. Zhuang, L. Nie, J. Zhang, Y. Zhang, N. Gu, T. Wang, J. Feng, D. Yang, S. Perrett, X. Yan, *Nat. Nanotechnol.*, 2007, **2**, 577-583.
- 36 C. K. Yee, R. Jordan, A. Ulman, H. White, A. King, M. Rafailovich, J. Sokolov, *Langmuir*, 1999, **15**, 3486-3491.
- 37 R. Hong, N. O. Fischer, T. Emrick, V. M. Rotello, *Chem. Mater.*, 2005, 17, 4617-4621.
- 38 A. H. Latham, M. E. Williams, *Langmuir*, 2006, **22**, 4319-4326.
- 39 C. Pale-Grosdemange, E. S. Simon, K. L. Prime, G. M. Whitesides, *J. Am. Chem. Soc.*, 1991, **113**, 12-20.
- 40 X. Xia, M. Yang, Y. Wang, Y. Zheng, Q. Li, J. Chen, Y. Xia, ACS Nano, 2012, 6, 512-522.
- 41 A. Bandyopadhyay, T. Das, S. Yeasmin, *Nanoparticles in Lung Cancer Therapy Recent Trends*, Springer, India, New Delhi, 2015.
- 42 M. Seehra, A. Bristow, *Noble and Precious Metals Properties, Nanoscale Effects and Applications*, IntechOpen, London, 2018.
- 43 Y. Xia, K. D. Gilroy, H. Peng, X. Xia, Angew. Chem. Int. Ed., 2017, 56, 60-95.
- 44 Y. Xia, X. Xia, H. Peng, J. Am. Chem. Soc., 2015, 137, 7947-7966.
- 45 Z. Xi, H. Ye, X. Xia, Chem. Mater., 2018, **30**, 8391–8414.
- 46 V. K. LaMer, R. H. Dinegar, J. Am. Chem. Soc., 1950, 72, 4847-4854.
- 47 D. Wang, T. Xie, Y. Li, Nano Res., 2009, 2, 30-46.
- 48 Y. Yin, A. P. Alivisatos, *Nature*, 2005, **437**, 664-670.
- 49 J. Zeng, Y. Zheng, M. Rycenga, J. Tao, Z. Li, Q. Zhang, Y. Zhu, Y. Xia, *J. Am. Chem. Soc.*, 2010, **132**, 8552-8553.

- 50 X. Xia, J. Zeng, B. McDearmon, Y. Zheng, Q. Li, Y. Xia, *Angew. Chem., Int. Ed.*, 2011, **52**, 12542-12546.
- 51 R. Long, S. Zhou, B. J. Wiley, Y. Xiong, Chem. Soc. Rev., 2014, 43, 6288-6310.
- 52 A. Ruditskiy, M. Zhao, K. D. Gilroy, M. Vara, Y. Xia, Chem. Mater., 2016, 28, 8800-8806.
- 53 X. Ye, L. Jin, H. Caglayan, J. Chen, G. Xing, C. Zheng, V. Doan-Nguyen, Y. Kang, N. Engheta, C. R. Kagan, C. B. Murray, *ACS Nano*, 2012, **6**, 2804-2817.
- 54 K. Pacławski, T. Sak, J. Min. Metall. Sect. B-Metall., 2015, **51**, 133-142.
- 55 Y. Xia, Y. Xiong, B. Lim, S. E. Skrabalak, Angew. Chem. Int. Ed., 2009, 48, 60-103.
- 56 A. R. Tao, S. Habas, P. Yang, *Small*, 2008, 4, 310-325.
- 57 J. Xie, S. Peng, N. Brower, N. Pourmand, S. X. Wang, S. Sun, *Pure Appl. Chem.*, 2006, **78**, 1003-1014.
- 58 Y. Wang, J. F. Wong, X. Teng, X. Z. Lin, H. Yang, Nano Lett., 2003, 3, 1555-1559.
- 59 J. Ge, Y. Hu, M. Biasini, C. Dong, J. Guo, W. P. Beyermann, Y. Yin, *Chem. Eur. J.*, 2007, **13**, 7153-7161.
- 60 J. F. Back, D. Oakenfull, M. B. Smith, *Biochemistry*, 1979, 18, 5191-5196.
- 61 A. D. Brown, J. R. Simpson, *Microbiology*, 1972, **72**, 589-591.
- 62 D. Caruntu, G. Caruntu, C. J. O'Connor, J. Phys. D: Appl. Phys., 2007, 40, 5801-5809.
- 63 S. E. Skrabalak, B. J. Wiley, M. Kim, E. V. Formo, Y. Xia, *Nano Lett.*, 2008, **8**, 2077-2081.
- 64 J. Park, J. Joo, S. G. Kwon, Y. Jang, T. Hyeon, *Angew. Chem. Int. Ed.*, 2007, **46**, 4630-4660.
- 65 Y. Wang, H. Peng, J. Liu, C. Z. Huang, Y. Xia, *Nano Lett.*, 2015, **15**, 1445-1450.
- 66 C. L. Lee, C. C. Wan, Y. Y. Wang, Adv. Func. Mater., 2001, 11, 344-347.
- 67 Y. Zheng, J. Tao, H. Liu, J. Zeng, T. Yu, Y. Ma, C. Moran, L. Wu, Y. Zhu, J. Liu, Y. Xia, *Small*, 2011, 7, 2307-2312.
- 68 X. Xia, J. Zeng, Q. Zhang, C. H. Moran, Y. Xia, J. Phys. Chem. C, 2012, 116, 21647-21656.
- 69 Y. Xiong, H. Cai, B. J. Wiley, J. Wang, M. J. Kim, Y. Xia, *J. Am. Chem. Soc.*, 2007, **129**, 3665-3675.
- 70 J. Xian, Q. Hua, Z. Jiang, Y. Ma, W. Huang, *Langmuir*, 2012, **28**, 6736-6741.
- 71 H. Zhang, M. Jin, Y. Xiong, B. Lim, Y. Xia, Acc. Chem. Res., 2013, 46, 1783-1794.
- 72 H. Wang, X. Qiao, J. Chen, X. Wang, S. Ding, *Mater. Chem. Phys.*, 2005, **94**, 449-453.
- 73 M. Jin, H. Liu, H. Zhang, Z. Xie, J. Liu, Y. Xia, *Nano Res.*, 2011, 4, 83-91.
- 74 M. Zawadzki, J. Okal, Mater. Res. Bull., 2008, 43, 3111-3121.

- 75 G. Frens, *Nat. Phys.*, 1973, **241**, 20-22.
- 76 D. S. Kilin, O. V. Prezhdo, Y. Xia, Chem. Phys. Lett., 2008, 458, 113-116.
- 77 N. G. Bastús, J. Comenge, V. Puntes, *Langmuir*, 2011, **27**, 11098-11105.
- 78 R. Fenger, E. Fertitta, H. Kirmse, A. F. Thünemann, K. Rademann, *Phys. Chem. Chem. Phys.*, 2012, **14**, 9343-9349.
- 79 Y. Wang, D. Aili, R. Selegård, Y. Tay, L. Baltzer, H. Zhang, B. Liedberg, *J. Mater. Chem.*, 2012, **22**, 20368-20373.
- 80 Z. Khan, S. A. Al-Thabaiti, A. Y. Obaid, A.O. Al-Youbi, *Colloids Surf. B*, 2011, **82**, 513-517.
- 81 Y. Zheng, X. Zhong, Z. Li, Y. Xia, Part. Part. Syst. Char., 2014, 31, 266-273.
- 82 J. Zhang, M. R. Langille, M. L. Personick, K. Zhang, S. Li, C. A. Mirkin, *J. Am. Chem. Soc.*, 2010, **132**, 14012-14014.
- 83 H. Yoo, M. H. Janga, Nanoscale, 2013, 5, 6708-6712.
- 84 Z. Gao, M. Xu, L. Hou, G. Chen, D. Tang, Anal. Chim. Acta, 2013, 776, 79-86.
- 85 G. T. Hermanson, *Bioconjugate Techniques*, 2nd ed., Academic Press, San Diego, 2008.
- 86 Y. Xiong, J. M. McLellan, Y. Yin, Y. Xia, Angew. Chem. Int. Ed., 2007, 46, 790-794.
- 87 Y. Xiong, H. Cai, Y. Yin, Y. Xia, Chem. Phys. Lett., 2007, 440, 273-278.
- 88 Y. Xiong, J. M. McLellan, J. Chen, Y. Yin, Z.-Y. Li, Y. Xia, *J. Am. Chem. Soc.*, 2005, **127**, 17118-17127.
- 89 Y. Xiong, I. Washio, J. Chen, H. Cai, Z.-Y. Li, Y. Xia, *Langmuir*, 2006, **22**, 8563-8570.
- 90 D. W. Oxtoby, *Nature*, 2000, **406**, 464-465.
- 91 G. C. Sosso, J. Chen, S. J. Cox, M. Fitzner, P. Pedevilla, A. Zen, A. Michaelides, *Chem. Rev.*, 2016, **116**, 7078-7116.
- 92 B. Lim, M. Jiang, P. H. C. Camargo, E. C. Cho, J. Tao, X. Lu, Y. Zhu, Y. Xia, *Science*, 2009, **324**, 1302-1305.
- 93 C. Chen, Y. Kang, Z. Huo, Z. Zhu, W. Huang, H. L. Xin, J. D. Snyder, D. Li, J. A Herron, M. Mavrikakis, M. Chi, K. L. More, Y. Li, N. M. Markovic, G. A. Somorjai, P. Yang, V. R. Stamenkovic, *Science*, 2014, **343**, 1339-1343.
- 94 M. Chen, B. Wu, J. Yang, N. Zheng, Adv. Mater., 2012, 24, 862-879.
- 95 H. Ataee-Esfahani, K. M. Koczkur, R. G. Weiner, S. E. Skrabalak, ACS Omega, 2018, 3, 3952-3956.
- 96 H. Zheng, R. K. Smith, Y. Jun, C. Kisielowski, U. Dahmen, A. P. Alivisatos, Science, 2009,

- **324**, 1309-1312.
- 97 C. Gao, J. Goeblb, Y. Yin, *J. Mater. Chem. C*, 2013, 1, 3898-3909.
- 98 N. R. Jana, L. Gearheart, C. J. Murphy, *Langmuir*, 2001, **17**, 6782-6786.
- 99 N. D. Burrows, A. M. Vartanian, N. S. Abadeer, E. M. Grzincic, L. M. Jacob, W. Lin, J. Li, J. M. Dennison, J. G. Hinman, C. J. Murphy, *J. Phys. Chem. Lett.*, 2016, 7, 632-641.
- 100 R. G. Chaudhuri, S. Paria, Chem. Rev., 2012, 112, 2373-2433.
- 101 M. B. Gawande, A. Goswami, T. Asefa, H. Guo, A. V. Biradar, D. Peng, R. Zboril, R. S. Varma, *Chem. Soc. Rev.*, 2015, **44**, 7540-7590.
- 102 S. Alayoglu, A. U. Nilekar, M. Mavrikakis, B. Eichhorn, Nature Mater., 2008, 7, 333-338.
- 103 J. Luo, L. Wang, D. Mott, P. N. Njoki, Y. Lin, T. He, Z. Xu, B. N. Wanjana, I.-I. S. Lim, C. Zhong, *Adv. Mater.*, 2008, **20**, 4342-4347.
- 104 T.-H. Yang, Y. Shi, A. Janssen, Y. Xia, Angew. Chem. Int. Ed., 2020, 59, 15378-15401.
- 105 W. A. Al-Saidi, H. Feng, K. A. Fichthorn, *Nano Lett.*, 2012, **12**, 997-1001.
- 106 H. Peng, S. Xie, J. Park, X. Xia, Y. Xia, J. Am. Chem. Soc., 2013, 135, 3780-3783.
- 107 H. Lee, S. E. Habas, S. Kweskin, D. Butcher, G. A. Somorjai, P. Yang, *Angew. Chem. Int. Ed.*, 2006, **45**, 7824-7828.
- 108 A. Yin, W. Liu, J. Ke, W. Zhu, J. Gu, Y. Zhang, C. Yan, *J. Am. Chem. Soc.*, 2012, **134**, 20479-20489.
- 109 S. Xie, H. Zhang, N. Lu, M. Jin, J. Wang, M. J. Kim, Z. Xie, Y. Xia, *Nano Lett.*, 2013, **13**, 6262-6268.
- 110 K. D. Gilroy, X. Yang, S. Xie, M. Zhao, D. Qin, Y. Xia, Adv. Mater., 2018, 30, 1706312.
- 111 X. Xia, S. Xie, M. Liu, H. Peng, N. Lu, J. Wang, M. J. Kim, Y. Xia, *Proc. Natl. Acad. Sci. U. S. A.*, 2013, **110**, 6669-6673.
- 112 E. Bauer, J. H. van der Merwe, Phys. Rev. B. Condens. Matter., 1986, 33, 3657-3671.
- 113 M. Copel, M. C. Reuter, E. Kaxiras, R. M. Tromp, *Phys. Rev. Lett.*, 1989, **63**, 632-635.
- 114 X. Xia, L. Figueroa-Cosme, J. Tao, H. Peng, G. Niu, Y. Zhu, Y. Xia, J. Am. Chem. Soc., 2014, 136, 10878-10881.
- 115 X. Xia, J. Zhang, N. Lu, M. J. Kim, K. Ghale, Y. Xu, E. McKenzie, J. Liu, H. Ye, *ACS Nano*, 2015, **9**, 9994-10004.
- 116 H. Ye, Q. Wang, M. Catalano, N. Lu, J. Vermeylen, M. J. Kim, Y. Liu, Y. Sun, X. Xia, *Nano Lett.*, 2016, **16**, 2812-2817.

- 117 Z. Gao, H. Ye, D. Tang, J. Tao, S. Habibi, A. Minerick, D. Tang, X. Xia, *Nano Lett.*, 2017, **17**, 5572-5579.
- 118 P. D. Josephy, T. Eling, R. P. Mason, J. Biol. Chem., 1982, 257, 3669-3675.
- 119 G. H, P. I, J. Clin. Chem. Clin. Biochem., 1985, 23, 453-460.
- 120 A. Frey, B. Meckelein, D. Externest, M. A. Schmidt, J. Immunol. Methods, 2000, 233, 47-56.
- 121 H. Mistry, F. Behafarid, E. Zhou, L. K. Ono, L. Zhang, B. R. Cuenya, *ACS Catal.*, 2014, 4, 109-115.
- 122 S. Mostafa, F. Behafarid, J. R. Croy, L. K. Ono, L. Li, J. C. Yang, A. I. Frenkel, B. R. Cuenya, *J. Am. Chem. Soc.*, 2010, **132**, 15714-15719.
- 123 M. Shao, T. Yu, J. H. Odell, M. Jin, Y. Xia, Chem. Commun., 2011, 47, 6566-6568.
- 124 R. Narayanan, M. A. El-Sayed, Nano Lett., 2004, 4, 1343-1348.
- 125 G. Fang, W. Li, X. Shen, J. M. Perez-Aguilar, Y. Chong, X. Gao, Z. Chai, C. Chen, C. Ge, R. Zhou, *Nat. Commun.*, 2018, **9**, 129.
- 126 Z. Gao, S. Lv, M. Xu, D. Tang, Analyst, 2017, 142, 911-917.
- 127 H. Ye, J. Mohar, Q. Wang, M. Catalano, M. J. Kim, X. Xia, Sci. Bull., 2016, 61, 1739-1745.
- 128 S. Wan, Q. Wang, H. Ye, M. J. Kim, X. Xia, Part. Part. Syst. Char., 2018, 35, 1700386.
- 129 C. N. Loynachan, M. R. Thomas, E. R. Gray, D. A. Richards, J. Kim, B. S. Miller, J. C. Brookes, S. Agarwal, V. Chudasama, R. A. McKendry, M. M. Stevens, *ACS Nano*, 2018, 12, 279-288.
- 130 C. Ge, R. Wu, Y. Chong, G. Fang, X. Jiang, Y. Pan, C. Chen, J. Yin, *Adv. Funct. Mater.*, 2018, 28, 1801484.
- 131 M. Nesselberger, S. Ashton, J. C. Meier, I. Katsounaros, K. J. J. Mayrhofer, M. Arenz, *J. Am. Chem. Soc.*, 2011, **133**, 17428-17433.
- 132 L. Bai, X. Wang, Q. Chen, Y. Ye, H. Zheng, J. Guo, Y. Yin, C. Gao, *Angew. Chem. Int. Ed.*, 2016, **55**, 15656-15661.
- 133 M. Shao, A. Peles, K. Shoemaker, Nano Lett., 2011, 11, 3714-3719.
- 134 W. Zhu, R. Michalsky, Ö. Metin, H. Lv, S. Guo, C. J. Wright, X. Sun, A. A. Peterson, S. Sun, J. Am. Chem. Soc., 2013, 135, 16833-16836.
- 135 C. Li, H. Tan, J. Lin, X. Luo, S. Wang, J. You, Y. Kang, Y. Bando, Y. Yamauchi, J. Kim, *Nano Today*, 2018, **21**, 91-105.
- 136 C. Li, M. Iqbal, J. Lin, X. Luo, B. Jiang, V. Malgras, K. C.-W. Wu, J. Kim, Y. Yamauchi, Acc.

- *Chem. Res.*, 2018, **51**, 1764-1773.
- 137 Z. Xi, W. Gao, X. Xia, ChemBioChem, 2020, 21, 2440-2444.
- 138 Y. Wang, A. Biby, Z. Xi, B. Liu, Q. Rao, X. Xia, ACS Appl. Nano Mater., 2019, 2, 4605-4612.
- 139 H. Wang, S. Xu, C. Tsai, Y. Li, C. Liu, J. Zhao, Y. Liu, H. Yuan, F. Abild-Pedersen, F. B. Prinz, J. K. Nørskov, Y. Cui, *Science*, 2016, **354**, 1031-1036.
- 140 L. Wang, Z. Zeng, W. Gao, T. Maxson, D. Raciti, M. Giroux, X. Pan, C. Wang, J. Greeley, *Science*, 2019, **363**, 870-874.
- 141 H. Huang, H. Jia, Z. Liu, P. Gao, J. Zhao, Z. Luo, J. Yang, J. Zeng, *Angew. Chem. Int. Ed.*, 2017, **56**, 3594-3598.
- 142 Y. Xiong, H. Shan, Z. Zhou, Y. Yan, W. Chen, Y. Yang, Y. Liu, H. Tian, J. Wu, H. Zhang,D. Yang, *Small*, 2017, 13, 1603423.
- 143 C. Kuo, L. K. Lamontagne, C. N. Brodsky, L. Chou, J. Zhuang, B. T. Sneed, M. K. Sheehan, C. Tsung, *ChemSusChem*, 2013, **6**, 1993-2000.
- 144 Z. Xi, X. Cheng, Z. Gao, M. Wang, T. Cai, M. Muzzio, E. Davidson, O. Chen, Y. Jung, S. Sun, Y. Xu, X. Xia, *Nano Lett.*, 2020, **20**, 272-277.
- 145 K. Kim, Appl. Microsc., 2015, 45, 101-105.
- 146 M. J. Hÿtch, E. Snoeck, R. Kilaas, *Ultramicroscopy*, 1998, **74**, 131-146.
- 147 Z. Niu, Y. Li, Chem. Mater., 2014, 26, 72-83.
- 148 A. Heuer-Jungemann, N. Feliu, I. Bakaimi, M. Hamaly, A. Alkilany, I. Chakraborty, A. Masood, M. F. Casula, A. Kostopoulou, E. Oh, K. Susumu, M. H. Stewart, I. L. Medintz, E. Stratakis, W. J. Parak, A. G. Kanaras, *Chem. Rev.*, 2019, 119, 4819-4880.
- 149 L. M. Rossi, J. L. Fiorio, M. A. S. Garcia, C. P. Ferraz, *Dalton Trans.*, 2018, 47, 5889-5915.
- 150 H. Ye, Y. Liu, A. Chhabra, E. Lilla, X. Xia, *ChemNanoMat*, 2017, **3**, 33-38.
- 151 B. Nikoobakht, M. A. El-Sayed, Langmuir, 2001, 17, 6368-6374.
- 152 H. Gao, H. Liu, H. Qian, G. Jiao, Z. Lu, *Phys. Chem. Chem. Phys.*, 2018, **20**, 1381-1394.
- 153 X. Qi, T. Balankura, Y. Zhou, K. A. Fichthorn, *Nano Lett.*, 2015, **15**, 7711-7717.
- 154 X. Xia, J. Zeng, L. K. Oetjen, Q. Li, Y. Xia, J. Am. Chem. Soc., 2012, **134**, 1793-1801.
- 155 Y. K. Du, P. Yang, Z. G. Mou, N. P. Hua, L. Jiang, J. Appl. Polym. Sci., 2006, 99, 23-26.
- 156 S. Kumar, J. Aaron, K. Sokolov, *Nat. Protoc.*, 2008, **3**, 314-320.
- 157 A. D. Friedman, S. E. Claypool, R. Liu, Curr. Pharm. Des., 2013, 19, 6315–6329.
- 158 X. Qian, X. Peng, D. O. Ansari, Q. Yin-Goen, G. Z. Chen, D. M. Shin, L. Yang, A. N. Young,

- M. D. Wang, S. Nie, Nat. Biotechnol., 2008, 26, 83-90.
- 159 M. J. Barry, N. Engl. J. Med., 2001, **344**, 1373-1377.
- 160 H. Lilja, D. Ulmert, A. J. Vickers, Nat. Rev. Cancer., 2008, **8**, 268-278.
- 161 A. Voller, D. E. Bidwell, A. Bartlett, *The enzyme linked immunosorbent assay (ELISA)*. A guide with abstracts of microplate applications. Dynatech Europe, Borough House, Rue du Pre., 1979.
- 162 N. Boonhama, J. Kreuzeb, S. Winterc, R. van der Vlugt, J. Bergervoetd, J. Tomlinson, R. Mumford. *Virus Res.*, 2014, **186**, 20-31.
- 163 D. E. Bidwell, A. A. Buck, H. J. Diesfeld, B. Enders, J. Haworth, G. Huldt, N. H. Kent, C. Kirsten, P. Mattern, E. J. Ruitenberg, A. Voller, *Bull World Health Organ.*, 1976, 54, 129-139.
- 164 J. Satija, N. Punjabi, D. Mishra, S. Mukherji, RSC Adv., 2016, 6, 85440-85456.
- 165 D. J. Porter, H. J. Bright, J. Biol. Chem., 1982, 258, 9913-9924.
- 166 D. A. Armbruster, M. D. Tillman, L. M. Hubbs, Clin. Chem., 1994, 40, 1233-1238.
- 167 G. A. Posthuma-Trumpie, J. Korf, A. van Amerongen, *Anal. Bioanal. Chem.*, 2009, **393**, 569-582.
- 168 D. Quesada-González, A. Merkoçi, Biosens. Bioelectron., 2015, 73, 47-63.
- 169 Y. Xu, Y. Liu, Y. Wu, X. Xia, Y. Liao, Q. Li, Anal. Chem., 2014, 86, 5611-5614.
- 170 K. Glynou, P. C. Ioannou, T. K. Christopoulos, V. Syriopoulou, *Anal. Chem.*, 2003, **75**, 4155-4160.
- 171 W. Zhou, X. Gao, D. Liu, X. Chen, Chem. Rev., 2015, 115, 10575-10636.
- 172 X. Yang, M. Yang, B. Pang, M. Vara, Y. Xia, Chem. Rev., 2015, 115, 10410-10488.
- 173 S. Eustis, M. A. El-Sayed, Chem. Soc. Rev., 2006, 35, 209-217.
- 174 T. Jiang, Y. Song, D. Du, X. Liu, Y. Lin, ACS Sens., 2016, 1, 717-724.
- 175 H. Ye, K. Yang, J. Tao, Y. Liu, Q. Zhang, S. Habibi, Z. Nie, X. Xia, ACS Nano, 2017, 11, 2052-2059.
- 176 J. Li, Z. Gao, H. Ye, S. Wan, M. Pierce, D. Tang, X. Xia, *Chem. Commun.*, 2017, **53**, 9055-9058.
- 177 Z. Gao, G. G. Liu, H. Ye, R. Rauschendorfer, D. Tang, X. Xia, *Anal. Chem.*, 2017, **89**, 3622-3629.
- 178 M. A. Mahmoud, R. Narayanan, M. A. El-Sayed, Acc. Chem. Res., 2013, 46, 1795-1805.

- 179 X. Xia, S. Choi, J. A. Herron, N. Lu, J. Scaranto, H. Peng, J. Wang, M. Mavrikakis, M. J. Kim, Y. Xia, *J. Am. Chem. Soc.*, 2013, **135**, 15706-15709.
- 180 L. Zhang, L. T. Roling, X. Wang, M. Vara, M. Chi, J. Liu, S. Choi, J. Park, J. A. Herron, Z. Xie, M. Mavrikakis, Y. Xia, *Science*, 2015, **349**, 412-416.
- 181 N. Lu, J. Wang, S. Xie, Y. Xia, M. J. Kim, Chem. Commun., 2013, 49, 11806-11808.
- 182 C. Ge, G. Fang, X. Shen, Y. Chong, W. G. Wamer, X. Gao, Z. Chai, C. Chen, J. Yin, *ACS Nano*, 2016, **10**, 10436-10445.
- 183 G. Fang, W. Li, X. Shen, J. M. Perez-Aguilar, y. Chong, X. Gao, Z. Chai, C. Chen, C. Ge, R. Zhou, *Nat. Commun.* 2018, **9**, 129.
- 184 G. Niu, L. Zhang, A. Ruditskiy, L. Wang, Y. Xia, Nano Lett., 2018, 18, 3879-3884.
- 185 A. M. Nightingale, J. H. Bannock, S. H. Krishnadasan, F. T. F. O'Mahony, S. A. Haque, J. Sloan, C. Drury, R. McIntyrec, J. C. deMello, *J. Mater. Chem. A*, 2013, **1**, 4067-4076.

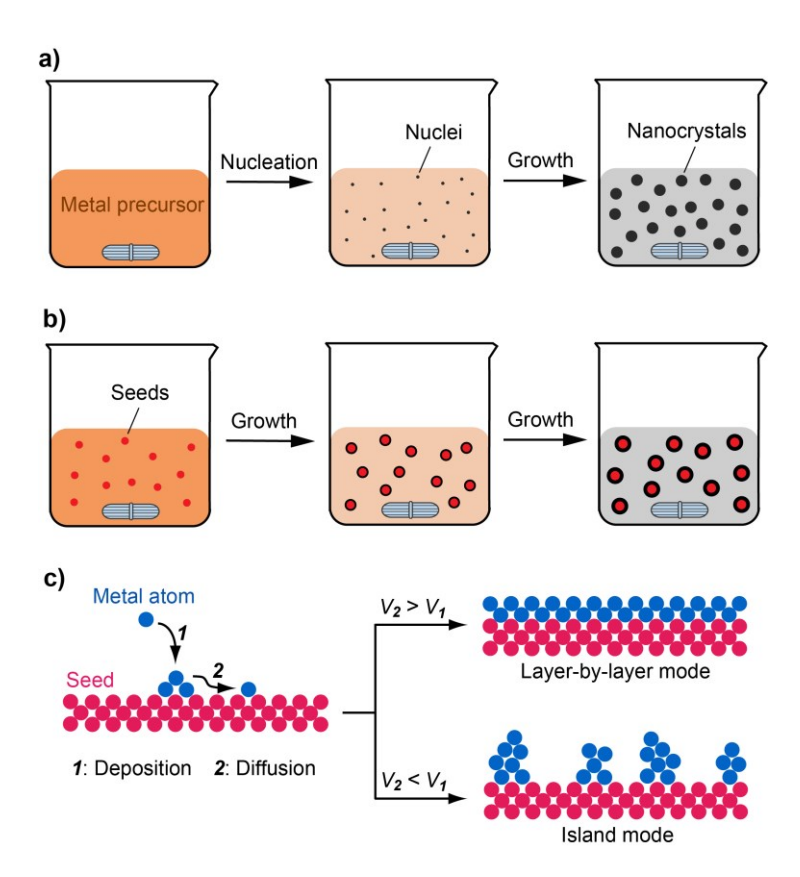


Figure 1. Schematics showing (a) one-pot synthesis and (b) seeded growth of PGM nanocrystals. (c) Atomic models showing two possible modes of deposition of metal atoms on a growing seed.

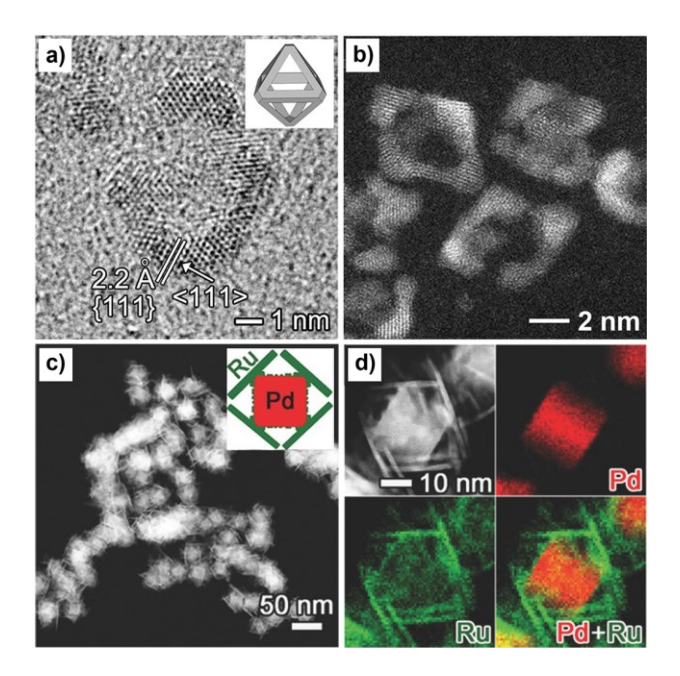


Figure 2. (a) High-resolution TEM (HRTEM) image and (b) high-angle annular dark-field scanning TEM (HAADF-STEM) image of Ru nanoframes. Reprinted with permission from ref 127. Copyright Springer Nature Switzerland AG. (c) HAADF-STEM image and (d) energy-dispersive X-ray (EDX) mapping images of Pd-Ru nanocrystals with a porous structure. Reprinted with permission from ref 128. Copyright 2018 Wiley-VCH.

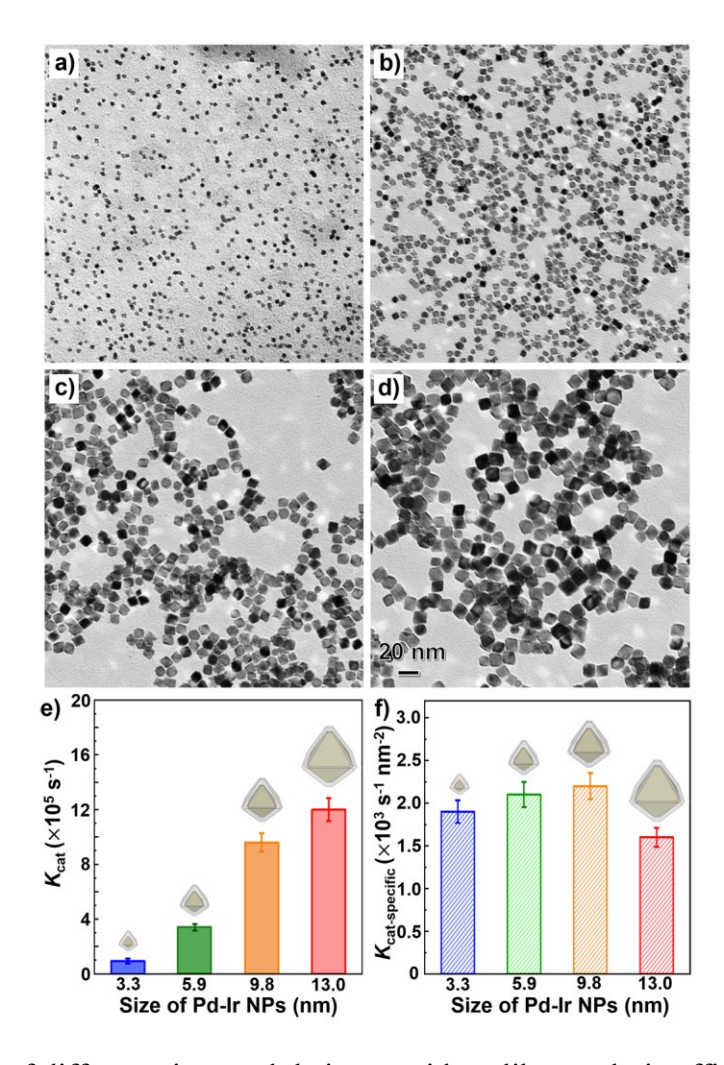


Figure 3. Pd-Ir NPs of different sizes and their peroxidase-like catalytic efficiencies. (a-d): TEM images of (a) 3.3 nm, (b) 5.9 nm, (c) 9.8 nm, and (d) 13.0 nm Pd-Ir NPs. (e, f): histograms comparing (e) K_{cat} and (f) $K_{\text{cat-specific}}$ values of Pd-Ir NPs of different sizes. Error bars indicate standard deviations of three independent measurements. Adapted with permission from ref 137. Copyright 2020 Wiley-VCH.

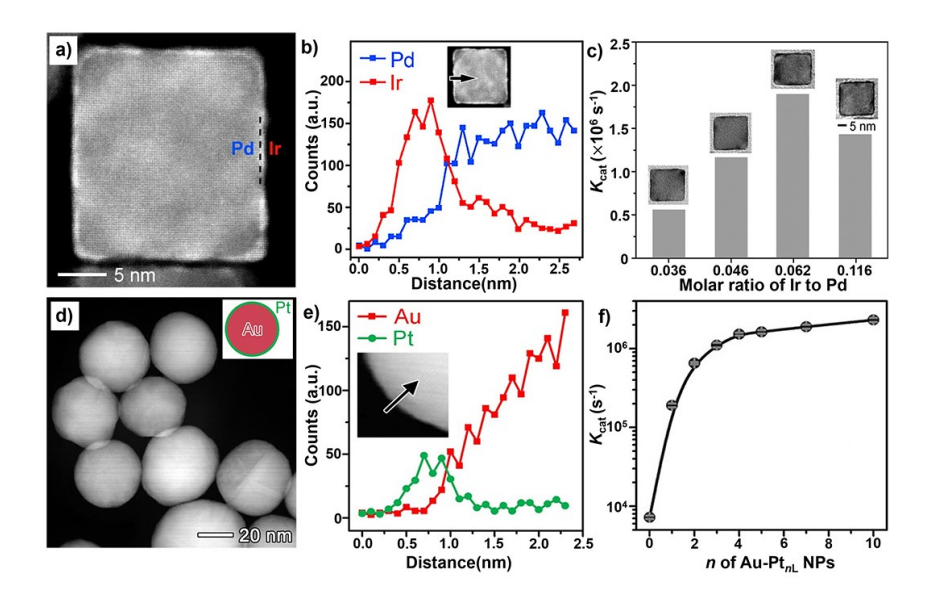


Figure 4. (a-c) Pd-Ir cubes and their peroxidase-like catalytic efficiencies: (a) HAADF-STEM image of an individual Pd-Ir cube; (b) Line-scan EDX spectra of elemental Pd and Ir recorded from an individual Pd-Ir cube (inset) along the direction as indicated by the black arrow; (c) A histogram comparing the K_{cat} values of Pd-Ir cubes with different molar ratios of Ir to Pd. Adapted with permission from ref 115. Copyright 2015 American Chemical Society. (d-f) Au-Pt_{nL} coreshell NPs (*n*L: *n* atomic layers of Pt) and their peroxidase-like catalytic efficiencies: (d) HAADF-STEM image of Au-Pt_{4L} NPs; (e) Line-scan EDX spectra of elemental Au and Pt recorded from an individual Au-Pt_{4L} NP (inset) along the direction as indicated by the black arrow; (f) A plot comparing the K_{cat} values of different Au-Pt_{nL} NPs. Adapted with permission from ref 117. Copyright 2017 American Chemical Society.

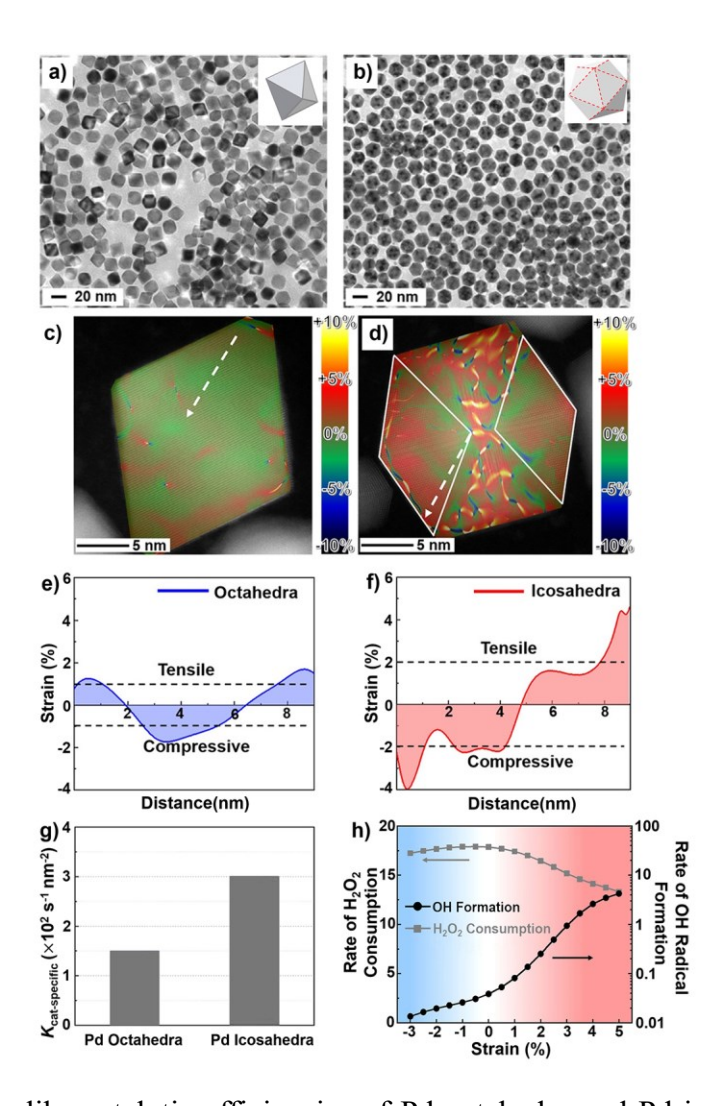


Figure 5. Peroxidase-like catalytic efficiencies of Pd octahedra and Pd icosahedra. (a,b): TEM images of (a) Pd octahedra and (b) Pd icosahedra. (c, d): Surface strain mapping for (c) Pd octahedron and (d) Pd icosahedron through geometric phase analysis. (e, f): Strain distribution along the white arrows shown in (c,d) for (e) Pd octahedron and (f) Pd icosahedron. (g) A histogram comparing the $K_{\text{cat-specific}}$ values of Pd octahedra and Pd icosahedra. (h) Simulated rates of OH radical formation and H₂O₂ consumption on Pd(111) as a function of surface strain from a microkinetic model based on self-consistent GGA-RPBE energies. Adapted with permission from ref 144. Copyright 2020 American Chemical Society.

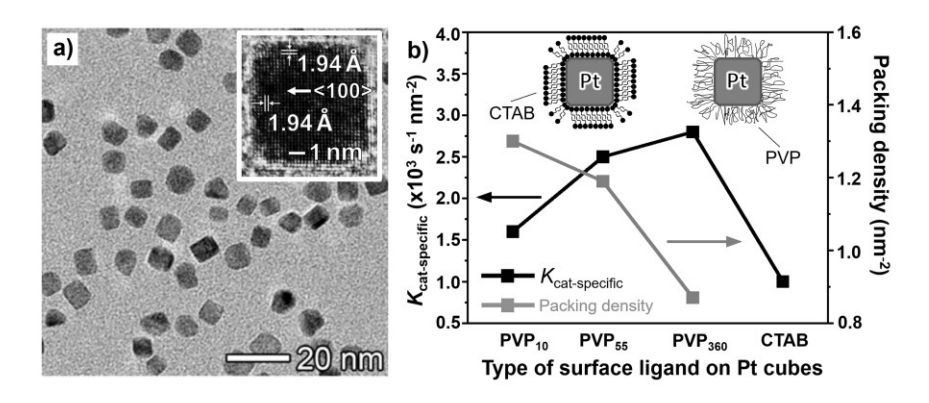


Figure 6. (a) TEM image along with a HRTEM image (inset) of PVP₅₅-capped Pt cubes. (b) Plots comparing the K_{cat} -specific values and packing densities of PVP₁₀-, PVP₅₅-, PVP₃₆₀, and CTAB-capped Pt cubes. Adapted with permission from ref 150. Copyright 2017 Wiley-VCH.

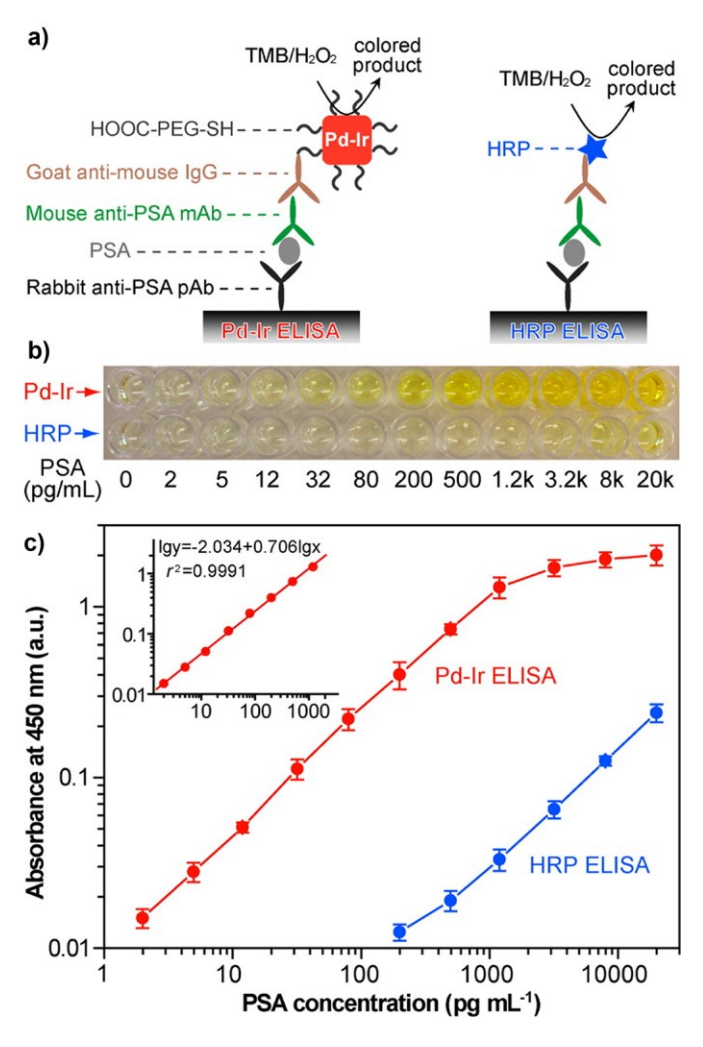


Figure 7. Comparison of Pd-Ir cubes based ELISA (Pd-Ir ELISA) and HRP based ELISA (HRP ELISA) in detecting PSA. (a) Schematics showing the principles of Pd-Ir and HRP ELISAs. (b) Representative photographs of the detection results of PSA standards with Pd-Ir and HRP ELISAs. (c) Calibration curves of the detection results in (b). Error bars indicate standard deviations of six independent measurements. Inset is the linear range region of the Pd-Ir ELISA. Reprinted with permission from ref 115. Copyright 2015 American Chemical Society.

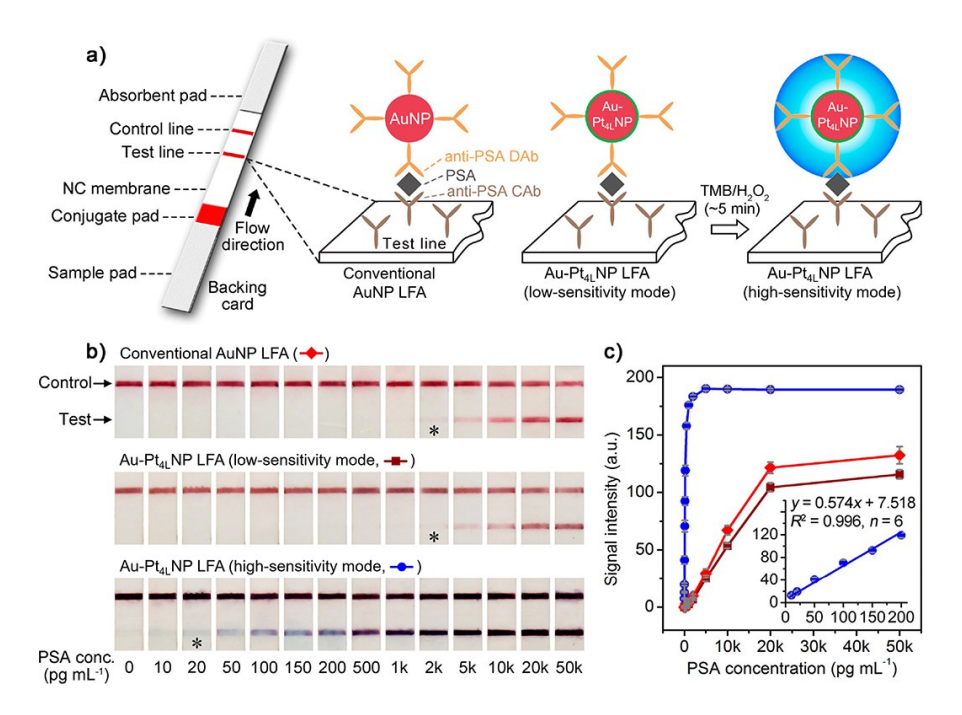


Figure 8. Comparison of AuNPs based LFA (AuNP LFA) and Au-Pt₄L NPs based LFA (Au-Pt₄L NP LFA) in detecting PSA. (a) Schematics showing the principles of AuNP and Au-Pt₄L NP LFAs. (b) Representative photographs of the detection results of PSA standards with AuNP and Au-Pt₄L NP LFAs. Asterisks (*) indicate detection limits by the naked eyes. (c) Calibration curves of the detection results in (b). Error bars indicate standard deviations of six independent measurements. Inset is the linear range region of the Au-Pt₄L NP LFA at high sensitivity mode. Reprinted with permission from ref 117. Copyright 2017 American Chemical Society.

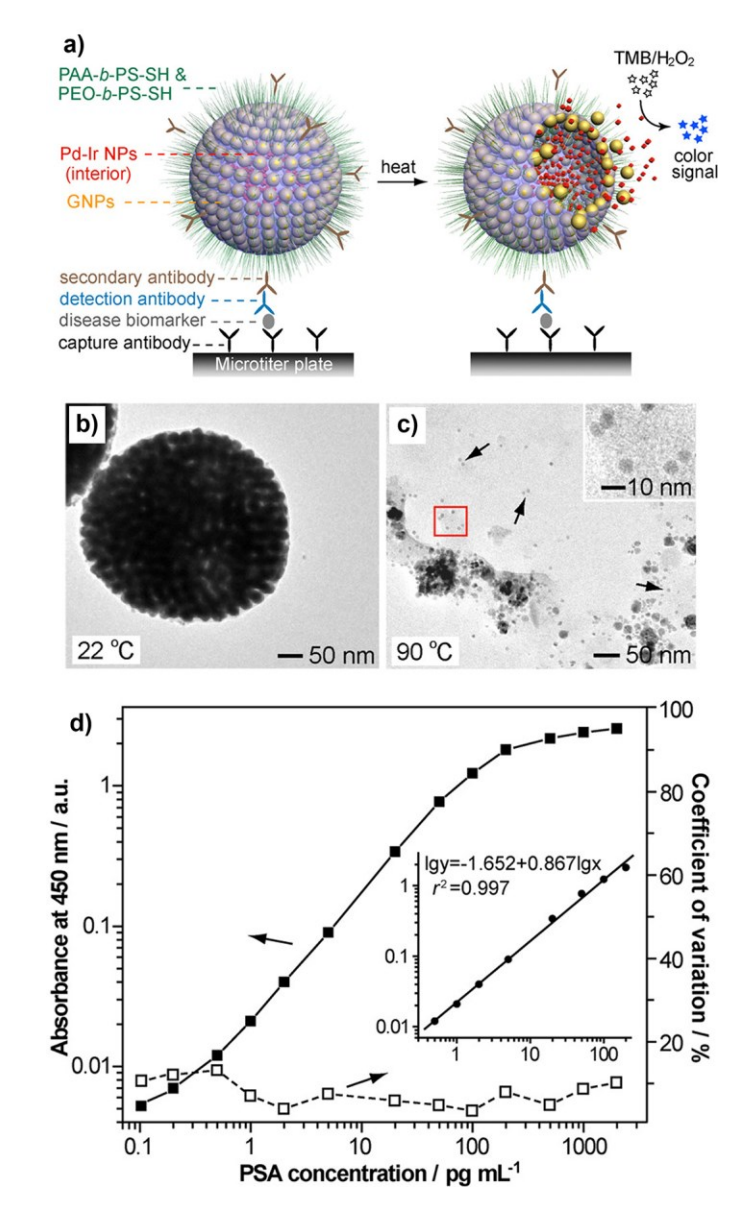


Figure 9. Pd-Ir NPs encapsulated GVs (Pd-Ir NPs@GVs) based ELISA. (a) Schematics showing the principle of Pd-Ir NPs@GVs based ELISA. (b, c) Representative TEM images of Pd-Ir NPs@GVs treated at different temperatures for 1 h: (b) 22 °C and (c) 70 °C. (d) Calibration curve of Pd-Ir NPs@GVs based ELISA of PSA standards. Inset shows the linear range region of the calibration curve. Reprinted with permission from ref 175. Copyright 2017 American Chemical Society.

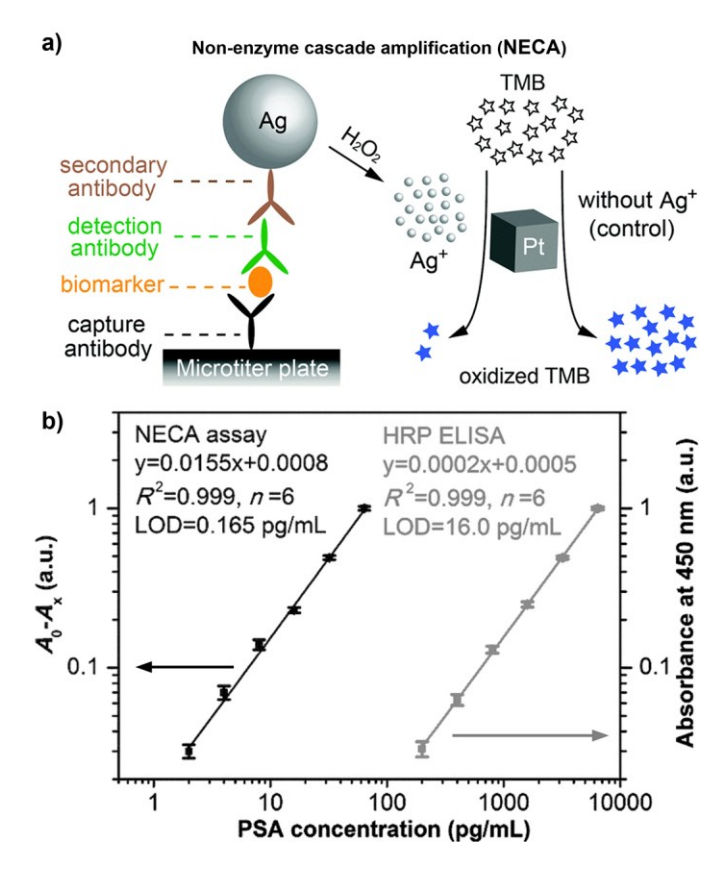


Figure 10. (a) Schematics showing the NECA assay of disease biomarker. (b) Calibration curves of NECA assay and HRP ELISA of PSA standards. Error bars indicate the standard deviations of six independent measurements. Adapted with permission from ref 176. Copyright 2017 Royal Society of Chemistry.